Soft Matter

ARTICLE TYPE

Cite this: DOI: 00.0000/xxxxxxxxxx

Dynamics of Prolate Spheroids in the Vicinity of an Air-Water Interface: Supplementary Information

Stefano Villa,[a] * Domenico Larobina,[b] Antonio Stocco,[c] Christophe Blanc,[d] Massimiliano M. Villone,[e] Gaetano D'Avino,[e] and Maurizio Nobili[d‡]

Received Date
Accepted Date

DOI: 00.0000/xxxxxxxxxx

1 Contributions of pendant drop's shape

As described in the Main Text, the geometry of the experimental setup is that of a pendant drop contained in a hollow glass cylinder closed on the top and opened on the bottom. Because of the pinning of the contact line on the cylinder lower edges, the air-water interface has a curvature that can be tuned by changing the amount of water contained in the cylinder. Both the optical analysis to recover the particle's coordinates and the interpretation of the measured dynamics in the Main Text are made assuming a flat air-water interface. The effect of the interface curvature must therefore be discussed, also taking into account its change over time due to water evaporation.

We first evaluated the evaporation by following over time the center of a pendant drop by moving the microscope focal plane with a piezoelectric actuator in order to always keep the air-water interface on focus. In this way we evaluated a displacement velocity of 0.2 μm/s of the interface due to evaporation, in a system where no precautions are taken to reduce evaporation. We then repeated the measurement by adding a protective flexible chamber as in Fig. 1 of the Main Text. The interface velocity in presence of the chamber is reduced to 0.05 μm/s. During the measurements we detected variations around this average of less than 10% for typical room temperature variations between 20°C and 28°C and relative humidity of 50-60% (the average at Montpellier, France). As a consequence, we estimate that during the time interval $10^3 - 10^4$ s of a typical experiment, the center of the pendant drop rises by about 0.05-0.5 mm. Since working with a perfectly flat interface for the entire duration of an experiment is not possible, in the experiment we use a convex interface in a way to bring particles towards the center of the drop where the interface is orthogonal to the optical axis. To ensure that the interface remains convex for all the experiment duration the center of the drop is initially fixed at an height 1 mm lower than the glass cylinder lower edges.

The interface curvature in principle affects the experimental data in two main ways. First, it introduces a tilt angle between the optical axis and the normal to the interface everywhere except for the drop's center, thus introducing a parallax error in the measurement of the displacement of x' and y', since this reference system parallel to the surface is different from the one of the image plane. To assess this contribution we evaluated the drop shape for the experimental parameters. Starting the experiment with ellipsoids near the drop center and considering the experimentally observed drifts, in the worst case scenario where the maximum observed drift moves the particle along the radial direction, the maximum distance from the drop center a particle can reach during its trajectory is still lower than 300 μm. The relative difference on the travelled distance in the image plane orthogonal to the optical axis and in a curved reference system of the drop is less then 0.01%, and thus negligible.

Besides for the parallax error, drop curvature in principle also affects particle dynamics as it introduces a confinement effect in the $x'y'$ plane. Because of the curvature radius much larger than the particle size, however, this effect is negligible as the MSDs appear linear with any saturation at large lag-time.

2 Details on the ellipsoids tracking

Dedicated algorithms have been designed specifically for the tracking of the interference pattern of ellipsoidal particles. The direction of the major axis projection on the plane parallel to the air-water interface is first found looking for the fringe pattern axial symmetry in the binarized version of the acquired image

[a] Max Planck Institute for Dynamics and Self-Organization, 37077 Göttingen, Germany.
[b] Institute of Polymers, Composites, and Biomaterials, National Research Council of Italy, Naples, 80055 Portici, Italy.
[c] Institut Charles Sadron, CNRS UPR22, University of Strasbourg, Strasbourg, France.
[d] Laboratoire Charles Coulomb (L2C), UMR 5221 CNRS-Université de Montpellier, Montpellier, France.
[e] Department of Chemical, Materials and Production Engineering, University of Naples Federico II, P.le Tecchio 80, 80125 Naples, Italy.
∗ E-mail: stefano.villa@ds.mpg.de
‡ E-mail: maurizio.nobili@umontpellier.fr

(Fig.2b of the Main Text). Binarization is made with an intensity threshold 50% larger than the average frame intensity, in order to only visualize the bright interference maxima. Such maxima are then identified as the regions of connected pixels having area larger than a given value. For each region we calculate the corresponding geometrical center. We then consider the ensemble of lines connecting couples of geometrical centers. Finally the fringe pattern major symmetry axis is selected as the line which minimizes the sum of line-geometrical centers distances. From the orientation of the found symmetry axis, the instantaneous value of the azimuthal angle ϕ is determined with a precision of about $0.3°$. A local Cartesian coordinates system xyz is also defined, where x is the direction parallel to the ellipsoids major axis, y is the orthogonal direction in the interface plane and z is the direction orthogonal to the interface.

In order to access the other degrees of freedom, for each frame i the intensity profile $I_i(\tilde{x})$ (Fig.S1) along the determined symmetry axis is extracted for both the blue and red channels of the camera. There, $\tilde{x}$ is defined as the distance from the center of the interference pattern $\tilde{x}=0$ along the symmetry axis. According to this definition, $\tilde{x}=0$ corresponds to the coordinate of the point of the ellipsoid closer to the air-water interface.

From each profile $I_i(\tilde{x})$, the positions $\tilde{x}_e$ of the intensity extrema (maxima and minima) are identified through a parabolic fit of the local maxima and minima and the ellipsoid profile $z_i(\tilde{x}_e)$ along its major axis is reconstructed (Fig.S1b). Reconstruction is made considering that between two adjacent extrema there is a difference in z of $\lambda/4n$, where λ is the light source wavelength and n is the water index of refraction. The reconstructed profile depends on the ellipsoid semi-axes a, b, the coordinates of its center of mass $\tilde{x}_0$, z_0, and its orientation given by the zenithal angle θ through the analytic expression:

$$z_i(\tilde{x}) = z_0 - \frac{\delta\tilde{x}\beta}{2\alpha} - \frac{\sqrt{\delta\tilde{x}^2\beta^2 - 4\alpha\left(\delta\tilde{x}^2\gamma - 1\right)}}{2\alpha}, \tag{S.1}$$

where $\delta\tilde{x} = (\tilde{x}-\tilde{x}_0)$ and α, β and γ are trigonometric functions of θ:

$$\alpha = \left(\frac{\sin\theta}{a}\right)^2 + \left(\frac{\cos\theta}{b}\right)^2 \tag{S.2}$$

$$\beta = 2\cos\theta\sin\theta\left(\frac{1}{b^2} - \frac{1}{a^2}\right)^2 \tag{S.3}$$

$$\gamma = \left(\frac{\cos\theta}{a}\right)^2 + \left(\frac{\sin\theta}{b}\right)^2 \tag{S.4}$$

In order to reduce the number of fitting parameters, they are recovered in two separated steps. First, for a given trajectory all the profiles $z_i(\tilde{x}_e)$ are averaged in order to obtain a single profile $Z(\tilde{x}_e)$ (Fig.S1c) having a zero zenithal angle ($\theta = \langle\theta\rangle = 0$) and zero $\tilde{x}_0$-position ($\tilde{x}_0 = \langle\tilde{x}_0\rangle = 0$). In this conditions the Eq.(S.1) results in:

$$z(\tilde{x}) = < z_0 > - b\sqrt{1 - \frac{\delta\tilde{x}^2}{a^2}} \tag{S.5}$$

The best fit of $Z(\tilde{x}_e)$ with Eq.S.5 allows to recover a and b with

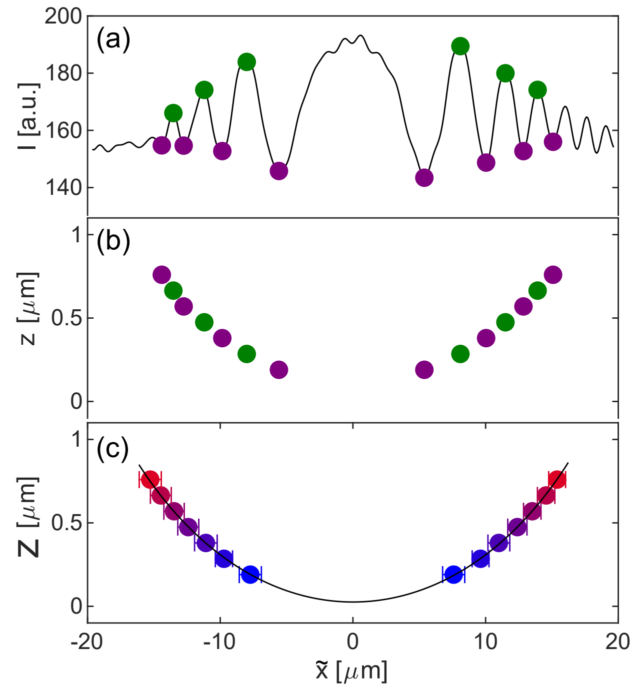

Fig. S 1 Reconstruction method to measure the semiaxes of an ellipsoid. (a) The position $\tilde{x}_e$ of the minima (violet points) and maxima (green points) along the ellipsoid's long axis is found. (b) Knowing the difference in z between two adjacent extrema is $\lambda/4n$, the $z(\tilde{x}_e)$ profile on the ellipsoid is reconstructed. (c) The latter operation is made for all frames on the same particle and the x'_e positions corresponding to the intensity extrema are obtained as a function of time. For each extremum the time average position is then evaluated (red-blue points). These are the points fitted (black line) to recover the moduli of the semiaxes of the ellipsoid. The orthogonal coordinates reported in (b,c) are the relative value of the particle-interface distance. The exact particle-interface distance is obtained adding integers multiples of $\lambda/2n$, where $m = 0, 1, ...$ is found by crossing the information coming from the two light sources as described in Refs. [1,2].

a relative precision of about 10%. Once the semi-axes are determined, single frame profiles $z_i(\tilde{x}_e)$ are fitted with Eq.S.1 reducing the free parameters to the instantaneous values of z_0, θ and $\tilde{x}_0$. The uncertainty over a and b mainly affects $\tilde{x}_{0,i}$ and θ, whose relative precision is of the same order of that of a. From the analysis of both red and blue channels, the orthogonal coordinate z_0 of the ellipsoid center mass is univocally determined frame by frame as described in Refs. [1,2] with a precision of few nanometers. From the position of $\tilde{x}_0$, the coordinates of the ellipsoid center of mass (x'_0, y'_0) in the laboratory reference system are obtained. Finally, the instantaneous displacements Δx_i and Δy_i between frame $i-1$ and frame i of the ellipsoid in the directions parallel and perpendicular to its major axis projection in the interface plane are retrieved as:

$$\Delta x_i = \Delta x'_i \cos\bar{\phi} + \Delta y'_i \sin\bar{\phi} \tag{S.6}$$

and

$$\Delta y_i = \Delta y'_i \cos\bar{\phi} - \Delta x'_i \sin\bar{\phi}, \tag{S.7}$$

with $\Delta x'_i = x'_{0,i} - x'_{0,i-1}$, $\Delta y'_i = y'_{0,i} - y'_{0,i-1}$ and $\bar{\phi} = (\phi_i + \phi_{i-1})/2$.

From the time evolution of the retrieved translational and rotational coordinates eventual drifts are removed by subtracting the average displacement. The instantaneous translational (v_x,v_y and v_z) and angular (ω and ω_ϕ) velocities are evaluated multiplying by the image acquisition frame rate the difference between two consecutive values of the correspondent coordinates.

3 Finite numerical aperture contribution to the interference pattern

In Fig.3a of the Main Text it can be seen a significant decrease of the interference pattern contrast when moving from the pattern center to the tips along the major axis. This can only in part be explained considering the limited coherence length of the light source. In general, indeed, several corrections have to be taken into account to quantitatively explain the intensity observed in DW-RIM. These points have been discussed by several authors for the quantitative determination of a z-profile in Reflection Interference Contrast Microscopy (RICM)[3]. This is very important in biophysics where the objectives are usually large with a high numerical aperture (NA>1), which strongly modulates the intensity contrast and stretches the interferogram.

Concerning our setup and experimental conditions, we have already discussed these effects for spheres imaged with a 100X long-working distance objective in a former work (see SI of Ref. [1]). There, we have shown that the positions of the visible interference maxima and minima were not very sensitive to the imperfect monochromaticity of the light. They were more sensitive to other effects such as the finite numerical aperture of the objective, which implies the presence of tilted incident rays incoherently interfering. Moreover, the curvature of the bead also modifies the tilt of the reflected rays depending on the point of incidence of the rays on the surface. Both phenomena were included in a numerical computation for the sphere. In the current work, these correction effects are weaker as we worked *(i)* with ellipsoids and *(ii)* with a long-working distance 50X objective with NA of 0.5 (illumination numerical aperture INA~ 0.45). With an ellipsoid, indeed, the curvature effect is much weaker since we study the interference only along the major axis in a limited region around the origin. Even considering an aspect ratio smaller than the lowest aspect ratio considered in the present work ($A \sim 5$), a bead of typical initial radius 4.35 μm gives an ellipsoid with the (relevant) principal curvature radius of 63 μm at the origin. At half semi-major axis distance, the tilt of the ellipsoid surface is only about 6°. Where the analysis stops (typically at $0.75a$) we found 13°. For the ellipsoid shown in Fig.S1 the values are respectively 3.8° and 7.4°.

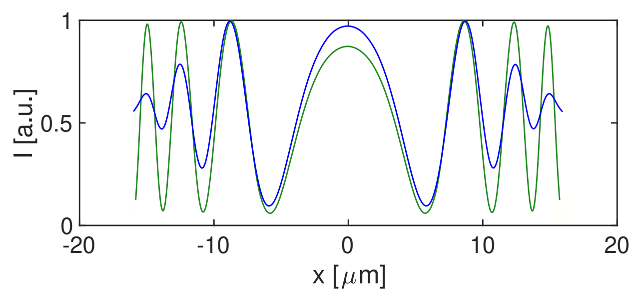

Fig. S 2 Simulated interference pattern along the major axis of an ellipsoid ($a = 21.6$ μm, $b = 2.46$ μm) located at 29 nm $+\tilde{m}_r\lambda_r/(2n)$ from the interface either considering (blue line) or not (green line) the effect of the experimental finite numerical aperture.

Due to the limited NA and INA< 0.5, we are closer to quasi-normal illumination and the stretching effects related to the NA can be neglected. For illustration, we computed the interference pattern along the major axis expected for the ellipsoid examined in Fig.S1, taking into account the finite numerical aperture of the objective. The result of the computation is compared in Fig.S2 with the one obtained in the simple normal illumination approximation (implicitly used in our data analysis approach). As it can be seen, the numerical aperture is responsible for a strong decrease of contrast but does not change significantly the position of the considered extrema, thus justifying the obliteration of finite NA contribution in the analysis of the experimental data.

4 Surface incompressibility and no-slip BC for an Ellipsoid

The 2D flow on the free interface induced by a vertical movement of an ellipsoidal particle is expected to have the same symmetry of the particle, *i.e.* elliptical. Using elliptical coordinates ν and μ along the confocal ellipses and hyperbolae respectively, the particle-induced flow field at the interface has components v_ν and v_μ. The symmetry of the problem imposes $v_\nu = 0$. The 2D incompressibility conditions results in:

$$v_\mu = \frac{K}{d\sqrt{\frac{1}{2}(\cosh 2\mu - \cos 2\nu)}}, \tag{S.8}$$

where K is an integration constant and d is the distance of one of the hyperbolae/ellipses focus with respect to the coordinate origin. In order to regularize the flow field v_μ at the origin ($\nu = \mu = 0$) one need to impose $K = 0$. As a result, the boundary conditions due to 2D flow incompressibility coincide with the ones of no-slip, i.e. $v_\nu = v_\mu = 0$.

5 Simulation details

The problem addressed in this work is a freely-buoyant rigid ellipsoid suspended in an incompressible Newtonian liquid in proximity of an air-water interface. A schematic representation of the investigated system is shown in Fig.1 of the Main Text. A Cartesian reference frame with the origin at the air-water interface and with the $z-$axis orthogonal to the interface is considered. The particle is positioned with its center of volume $\mathbf{r}$ on the $z-$axis. The normalized distance between the particle center of volume and the interface is defined as $h = z_0/2b$, and the angle between the spheroid major axis and the interface normal vector $\mathbf{n}$ is denoted with θ. Without loss of generality, the x-axis of the reference frame is selected coinciding with the projection along z of the ellipsoid major axis on the interface. The spheroid aspect ratio is defined as $A = a/b$, with a and b the major and minor semi-axes, respectively.

Assuming creeping flow conditions and incompressible Newtonian fluid, the fluid dynamics governing equations are given by:

$$\nabla \cdot \mathbf{v} = 0 \tag{S.9}$$

$$\nabla \cdot \sigma = -\nabla p + \mu \nabla^2 \mathbf{v} = \mathbf{0} \tag{S.10}$$

where $\sigma = -p\mathbf{I} + 2\mu\mathbf{D}$ is the stress tensor with $\mathbf{D}$ the rate-of-deformation tensor and $\mathbf{I}$ the unity tensor, $\mathbf{v}$, p, and μ are the velocity, pressure, and viscosity of the fluid, respectively.

The boundary conditions read as:

$$\mathbf{v} = \mathbf{u} + \omega \times (\mathbf{r}_s - \mathbf{r}) \qquad \text{on } \Gamma_p \tag{S.11}$$

$$\mathbf{v} = \mathbf{0} \qquad \text{on } \Gamma_w \tag{S.12}$$

where $\mathbf{r}_s - \mathbf{r}$ denotes the distance vector of a point $\mathbf{r}_s$ on the ellipsoid surface from the ellipsoid center of volume, $\mathbf{u}$ and ω are the particle translational and rotational velocities, Γ_p is the particle surface, and Γ_w collects all the external boundaries of the computational domain except the interface (corresponding to the xy-plane). The first equation accounts for the rigid-body motion of the particle, whereas the second equation expresses the quiescent conditions of the fluid ‘far’ from the particle.

The air-water interface, denoted by Γ_s, is assumed to be flat and a perfect slip condition is applied[4]:

$$\mathbf{v} \cdot \mathbf{n} = 0 \qquad \text{on } \Gamma_s \tag{S.13}$$

$$(\mathbf{I} - \mathbf{nn}) \cdot (\sigma \cdot \mathbf{n}) = \mathbf{0} \qquad \text{on } \Gamma_s \tag{S.14}$$

In this work, we will also investigate the effect of the no-slip condition Eq. (S.12) at the interface.

Finally, under inertialess conditions, the force and torque acting at the particle surface are:

$$\mathbf{F} = \int_{\Gamma_p} \sigma \cdot \mathbf{n} \, d\Gamma_p \tag{S.15}$$

$$\mathbf{T} = \int_{\Gamma_p} (\mathbf{r}_s - \mathbf{r}) \times (\sigma \cdot \mathbf{n}) \, d\Gamma_p \tag{S.16}$$

where $\mathbf{n}$ is the local normal to the particle surface, pointing to the fluid.

We solve the governing equations by applying a single non-zero component of the combined force/torque vector $(\mathbf{F}, \mathbf{T})$ and compute the six components of the translational and rotational velocity vector $(\mathbf{u}, \omega)$ as discussed in the Main Text.

The system of equations is numerically solved by a standard Galerkin-Finite Element method in the cubic box with length L[5]. A boundary-fitted mesh with tetrahedral elements is used. A quadratic continuous interpolation (P2) is used for the velocity and a linear continuous interpolation (P1) is used for the pressure. Mesh convergence has been verified for all the calculations presented in this work. A finer mesh is required when the particle is close to the interface in order to accurately solve the fields between the spheroid and the interface. The total number of elements varies between about 70000 and 160000. To guarantee unperturbed conditions far from the particle, the length L must be chosen sufficiently larger than the particle size. We found that a value of $L = 20a$ is sufficient to neglect the effects of the virtual walls.

Notes and references

1 S. Villa, A. Stocco, C. Blanc and M. Nobili, *Soft Matter*, 2020, **16**, 960–969.

2 S. Villa, C. Blanc, A. Daddi-Moussa-Ider, A. Stocco and M. Nobili, *Journal of Colloid and Interface Science*, 2023, **629**, 917–927.

3 L. Limozin and K. Sengupta, *ChemPhysChem*, 2009, **10**, 2752–2768.

4 D. Leonardo, D. R., L. D., Angelani and V. Lebba, *Phys. Rev. Lett.*, 2011, **106**, 038101.

5 J. N. Reddy and D. K. Gartling, *The finite element method in heat transfer and fluid dynamics*, CRC press, 2010.

	A	a [μm]	b [μm]	$r_{eq}=a^{1/3}b^{2/3}$ [μm]	z_{gap} [nm]	$M_{a,xx}/2b\eta$	$M_{a,yy}/2b\eta$	$M_{a,zz}/2b\eta$	$M_{c,zz}/(2b)^3\eta$	$M_{c,yy}/(2b)^3\eta$
1	6	14	2.4	4.3	980	0.05	0.033	0.0019	0.0053	0.0006
2	6.2	16	2.6	4.8	943	0.085	0.033	0.00046	0.006	0.0004
3	6.7	16	2.4	4.5	876	0.11	0.037	0.0027	0.0042	0.0003
4	6.9	18	2.6	5	629	0.15	0.033	0.0016	0.007	0.00057
5	7	19	2.7	5.1	690	-	0.015	0.002	0.0034	-
6	7.1	20	2.8	5.5	1.12e+03	0.16	0.045	0.0014	0.0023	0.0012
7	7.1	19	2.7	5.1	747	0.06	0.031	0.0023	0.0061	0.00039
8	7.6	20	2.6	5.1	642	-	0.015	0.0019	0.0036	-
9	8.3	18	2.2	4.5	786	0.12	0.041	0.0021	0.0046	0.00011
10	9.3	20	2.2	4.6	741	-	0.027	0.0019	0.0039	0.0005
11	9.4	20	2.2	4.6	786	0.078	-	0.0019	0.0011	0.00025
12	9.5	22	2.3	4.8	773	0.075	0.035	0.0016	0.0035	0.00026
13	9.5	20	2.1	4.5	935	-	-	0.0016	0.0038	-
14	9.8	20	2.1	4.5	811	0.063	0.017	0.0021	0.0014	0.0004
15	10	22	2.2	4.7	709	0.13	0.029	0.0011	0.0022	0.00013
16	12	23	1.9	4.3	808	-	-	0.0016	0.00068	-
17	12	21	1.7	3.9	860	0.096	-	0.0023	0.0019	-
18	12	22	1.8	4.1	755	0.089	0.013	0.0017	0.00061	0.0001

Fig. S 3 Supplementary table. Experimental data for each single measured ellipsoids reported for increasing aspect ratio. In the columns are reported: the aspect ratio A, the major (a) and the minor (b) semi-axes, the radius r_{eq} of a sphere of same volume, the particle-interface average gap distance z_{gap} and the five measured normalized mobilities with a normalisation factor of $2b\eta$ (translational mobilities) and $(2b)^3\eta$ (rotational mobilities). Missing values correspond to datasets where noise makes the MSD analysis unreliable. Those elements are excluded from the averages reported in the Main Text.